

On the effect of temperature and strain-rate dependent viscosity on global mantle flow, net rotation, and plate-driving forces

Thorsten W. Becker

Department of Earth Sciences, University of Southern California, 3651 Trousdale Parkway, Los Angeles CA 90089-0740, USA. E-mail: twb@usc.edu

Accepted 2006 July 31. Received 2006 July 28; in original form 2006 April 27

SUMMARY

Global circulation models are analysed using a temperature and strain-rate dependent rheology in order to refine previous estimates of the nature of mantle flow and plate driving forces. Based on temperature inferred from a tectonic model and seismic tomography, the suboceanic viscosity is lower than underneath continents by \sim one order of magnitude. If net-rotations of the lithosphere with respect to a stable lower mantle reference frame are accounted for, the patterns of flow in the upper mantle are similar between models with layered and those with laterally varying viscosity. The excited net rotations scale with the viscosity contrast of continental roots to the ambient mantle; this contrast is dynamically limited by the power-law rheology. Surface net rotations match the orientation of hotspot reference-frame Euler poles well, and amplitudes are of the right order of magnitude. I compare prescribed surface velocity models with free-slip computations with imposed weak zones at the plate boundaries; velocity fields are generally consistent. Models based on laboratory creep laws for dry olivine are shown to be compatible with average radial viscosity profiles, plate velocities in terms of orientation and amplitudes, plateness of surface velocities, toroidal:poloidal partitioning, and fabric anisotropy formation under dislocation creep in the upper mantle. Including temperature-dependent variations increases the relative speeds of oceanic *versus* continental lithosphere, makes surface velocities more plate-like, and improves the general fit to observed plate motions. These findings imply that plate-driving force studies which are based on simpler mantle rheologies may need to be revisited.

Key words: mantle convection, plate driving forces, seismic anisotropy.

1 INTRODUCTION

Global mantle flow models explain a wide range of geophysical and geological observations based on seismic tomography and plate configurations (e.g. Hager & O'Connell 1981; Hager & Clayton 1989; Ricard & Vigny 1989; Forte & Mitrovica 2001). Recently, computations were used, for example, to address long-standing questions about the partitioning of driving forces (Forsyth & Uyeda 1975; Chapple & Tullis 1977) by combining viscous flow and edge-force approaches (Becker & O'Connell 2001; Conrad & Lithgow-Bertelloni 2004). Given the general success of global flow models in large-scale mantle convection applications, the range of predicted synthetics for model verification has also been expanded to include, for instance, seismic anisotropy (e.g. Gaboret *et al.* 2003; Becker *et al.* 2003; Behn *et al.* 2004). It is, therefore, important to investigate the common rheological assumptions of mantle circulation models further in order to evaluate the robustness of the results, particularly with regard to the predicted flow at the surface and at depth. Here, I mainly focus on large-scale patterns and analyse how velocities throughout the mantle are modified from models with only radially varying viscosity if lateral viscosity variations (LVVs) are incorporated. LVVs are well studied in Cartesian models in

2- and 3-D. There have also been previous studies of global, spherical mantle flow with LVVs for Newtonian creep (Martinec *et al.* 1993; Zhang & Christensen 1993; Wen & Anderson 1997; Zhong & Davies 1999; Zhong *et al.* 2000; Zhong 2001; Yoshida *et al.* 2001; Čadek & Fleitout 2003; Conrad & Lithgow-Bertelloni 2006). However, we expect that the upper mantle exhibits power-law creep behaviour with additional strain rate, $\dot{\epsilon}$, dependence of the viscosity (e.g. Ranalli 1995). Upper mantle anisotropy is likely formed by progressive deformation of olivine under dislocation creep (e.g. Nicolas & Christensen 1987). Particularly for seismic anisotropy studies, the inclusion of power-law viscosity in flow models may, therefore, be of essence to be consistent with regard to model assumptions. In 3-D Cartesian, models with non-Newtonian rheologies have recently focused on the excitation of plate-like flow (e.g. Tackley 2001a; Tackley 2001b; Stein *et al.* 2004). However, I am only aware of one study that addresses 3-D spherical power-law flow, Čadek *et al.* (1993). This study was restricted to small LVVs and low degree spherical harmonics resolution. Čadek *et al.* found that velocities were more sensitive to rheology than the geoid. It was also shown that the introduction of power-law flow led to excitation of toroidal motion, though at very low amplitude, consistent with Zhang & Christensen (1993) findings.

Since a comprehensive study on the role of rheology for mantle flow in the present-day plate-tectonic setting at higher resolution is still missing, I analyse global, temperature-dependent, power-law flow models, building on Becker *et al.* (2006b), Becker *et al.* (2006a). We found that variations in large-scale flow fields due to the rheological assumptions are on average less important than other uncertainties such as the inferred density structures. In a related study, Conrad & Lithgow-Bertelloni (2006) recently analysed the effect of temperature-dependent viscosity on the viscous tractions that are exerted on the lithosphere by mantle flow. These authors found that the directions of shear vary little as a function of viscosity variations, but the drag amplitudes increase with the relative viscosity contrast of strong subcontinental roots. The present study follows up on Zhong (2001) (hereafter: ZH01), Čadež & Fleitout (2003) and Conrad & Lithgow-Bertelloni (2006) work, and is in essence an abridged, spherical version of the seminal study by Christensen (1984). He found that 2-D convection with temperature and strain-rate dependent viscosity is similar to Newtonian flow for certain conditions. Substantiating earlier 2-D and 3-D work, I show that the effect of power-law induced variations is indeed moderate in terms of changing the patterns of global mantle flow. This is particularly the case for the uppermost mantle, which is presumably most important for studies of seismic anisotropy. I study both models with prescribed plate motions, and ‘self-consistent’ models with a free-slip mechanical boundary condition on top and imposed weak zones along plate boundaries. ‘Self-consistent’ here means force-equilibrium for the entirely density-driven free-slip models, not a consistent generation of plates and plate boundaries, which I do not attempt here (see e.g. Bercovici *et al.* 2000, for a discussion). As LVV’s can potentially excite net motion of the mantle, the proper reference frame becomes an issue. However, if mean rotations are corrected for, the results are consistent for both approaches.

My results lend confidence in the gross conclusions of earlier work using global flow models. In terms of the fit to observed plate motions, models with LVV’s due to temperature-dependent creep are more Earth-like. While LVV’s do modify the flow, especially with regard to amplitudes, the flow geometry effects are probably most important for regional, or higher-resolution applications.

2 METHODS

2.1 Model set-up

Mantle convection is approximated by solving the equations for instantaneous, incompressible, infinite Prandtl number, fluid flow (e.g. Zhong *et al.* 2000). Following Conrad & Lithgow-Bertelloni (2006), internal density and rheological anomalies are inferred based on a combination of seismic tomography, seafloor age and a tectonic model. The idea is to study the effect of LVV’s for a generic set-up that purposefully does not account for details, such as shallow structure within oceanic plates (e.g. Ritzwoller *et al.* 2004). Underneath oceanic regions in the upper boundary layer, Müller *et al.* (1997) and the 3SMAC (Nataf & Ricard 1996) interpolation are used for seafloor ages, t , to assign a half-space cooling profile with non-dimensional temperature $T(t, z) = \text{erf}(z/(2\sqrt{\kappa t}))$. Here, z is depth, and κ thermal diffusivity (see Table 1 for model parameters). The maximum oceanic plate ‘thickness’ (depth where $T = 0.95$) is limited to 100 km. Underneath continents, the lithospheric thickness is estimated by finding the depth up to which seismic tomography consistently shows a fast shear wave, v_S , anomaly of $d \ln v_S = 2$ per cent. I mostly use the composite model *smean* of Becker & Boschi (2002) as a reference for velocity anomalies of the mantle.

Table 1. Dynamic model parameters. The Rayleigh number is defined using the Earth’s radius as in Zhong *et al.* (2000).

Parameter	Symbol	Value
Density/velocity anomaly	$D = \frac{d \ln \rho}{d \ln v_S}$	0.15
Scaling		
Thermal diffusivity	κ	$10^{-6} \text{ m}^2 \text{ s}^{-1}$
Thermal expansivity	α	$2 \cdot 10^{-5} \text{ K}^{-1}$
Scaling temperature difference	ΔT	1785° K
Non-dimensional temperature	T	
Non-dimensional reference (background) temperature	T_c	1
Non-dimensional temperature	$\frac{dT}{d \ln v_S} = -\frac{D}{\alpha \Delta T}$	-4.2
Anomaly scaling, $T = T_c + dT$		
Gravitational acceleration	g	10 m s^{-2}
Reference density	ρ	3300 kg m^{-3}
Reference viscosity	η_0	$2 \times 10^{21} \text{ Pa s}$
Earth’s radius	R	6371 km
Rayleigh number	$Ra = \frac{g \alpha \rho \Delta T R^3}{\kappa \eta_0}$	$1.5 \cdot 10^8$

Half-space cooling profiles with pseudo-ages are then fit (Conrad & Lithgow-Bertelloni 2006), roughly matching these depths up to a maximum thickness of 300 km.

Above 300 km, this temperature model will be used for temperature-dependent viscosities and the deviations from a layer mean for thermal buoyancy. The exceptions are ‘continental roots’, which here refers to relatively stiff, cold, and long-lived regions underneath old continental plates (Jordan 1978). Since continental roots appear fast in tomography but may be overall neutrally buoyant, I set the buoyancy effect of the upper 300 km smoothly to zero underneath continental regions that have a significant fast v_S anomaly at ~ 100 km depth (Fig. 1). Masking out continental

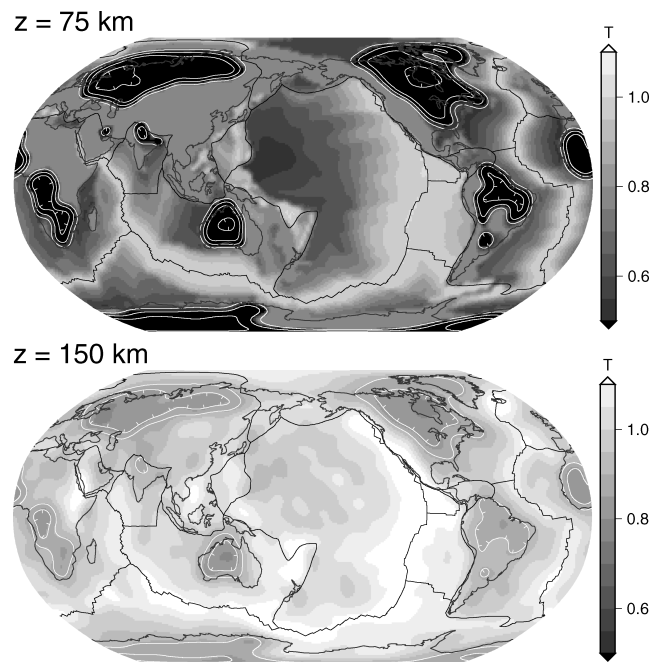


Figure 1. Inferred temperature (shading) and compositional anomalies (contours) of the geodynamic input model at depths of 75 (top) and 150 km (bottom). Plots show non-dimensional T as inferred from seafloor age and seismic tomography in a Pacific centred view. White contour lines show composition c at 0.2 intervals ($c \in [0;1]$) delineating continental roots. Heavy black lines denote NUVEL-1 plate boundaries.

roots introduces a compositional anomaly, c , which modifies any temperature anomaly $dT|_0$ as $dT = cdT|_0$. The c parameter is unity everywhere below 300 km and tends toward zero inside old continental regions. The transition is smoothed from 300 km depth to the surface in order to not induce sharp jumps (Fig. 1). Below 100 and 300 km for oceanic and continental regions, respectively, all variations from the constant background temperature are inferred from seismic tomography. My parameter choices are guided by results of previous flow models, including Becker & O'Connell (2001). For sublithospheric buoyancy anomalies, *smean* is used for most models and scaled by a typical density/velocity anomaly conversion factor with the model parameters given in Table 1.

The mechanical boundary conditions of the flow computations are free-slip at the core–mantle boundary (CMB), and either prescribed plate-motions, or free-slip at the surface. For the prescribed velocity models, I use a degree $\ell_{\max} = 63$ spherical harmonic expansion of NUVEL-1 plate motions (DeMets *et al.* 1990) in the no-net-rotation (NNR) reference frame, for consistency with older models and to smooth the plate boundary transition. Convection with only radial viscosity variations does not excite toroidal flow (e.g. Bercovici *et al.* 2000). In particular, without LVVs there cannot be any net motions (or rotations, NR) the entire lithosphere with respect to the lower mantle (Ricard *et al.* 1991; O'Connell *et al.* 1991). The surface NNR reference frame was thus a natural choice for Hager & O'Connell (1981) type flow models without LVVs, but should probably be abandoned if LVVs are included (*cf.* Zhong 2001). As I show below, NR flow with respect to the fixed surface NNR velocities is indeed induced for models with prescribed plate motions. This leads to significantly different velocity fields for LVVs if this effect is not corrected for.

For the free-slip models, I impose weak zones along the plate boundaries to facilitate plate-like motion at the surface (e.g. Zhong *et al.* 2000). By comparison of such purely density-driven flow with the prescribed velocity models one can check if the latter are in force-equilibrium. For free-slip models, one can also compare the variations in velocities as a function of rheology in a more consistent reference frame with regard to net motions. Following ZH01, I compute NR flow by spherical harmonic analysis of the numerical velocity solution in each layer. The NR Euler vector at depth z shall be given by $\omega(z)$. A mean, whole mantle NNR reference frame (MM–NNR) can then be calculated from the average NR

$$\bar{\omega} = \frac{1}{z_c} \int_0^{z_c} \omega(z) dz. \quad (1)$$

Table 3. Rheological models used, laws A and B refer to eqs (2) and (4), respectively. Models 1–4 were constructed to isolate the effects of T and $\dot{\epsilon}$ -dependence, and the η_{eff} model is based on dry olivine parameters from Hirth & Kohlstedt (2004). Parameters choices and A' scaling for η_{eff} are discussed in the Appendix.

Model	Rheological		A'	n	m	d	E	E^*	V^*			
	Type	Symbol								Depth range	Law	[$10^{-15} \frac{\text{m}^m}{\text{Pa}^m \text{s}}$]
1	Layered	η_r	global	A	–	–	–	0	–	–		
2	Strain-rate dependent	$\eta(\dot{\epsilon})$	$0 \text{ km}^a \leq z \leq 410 \text{ km}$	A	–	3	–	–	0	–		
			$z > 410 \text{ km}$	A	–	1	–	–	0	–		
3	Temperature dependent	$\eta(T)$	Global	A	–	1	–	–	30	–		
4	Temperature and strain-rate dependent	$\eta(T, \dot{\epsilon})$	$0 \text{ km}^a \leq z \leq 410 \text{ km}$	A	–	3	–	–	30	–		
			$z > 410 \text{ km}$	A	–	1	–	–	30	–		
5	Laboratory-derived olivine creep law	η_{eff}	$z \leq 660 \text{ km}$, dislocation	B	4.5	3.5	0	–	–	530	14	
			$z \leq 660 \text{ km}$, diffusion	B	7.4	1	3	5	–	–	375	6
			$z > 660 \text{ km}$	A	–	1	–	–	–	30	–	

^a: Power law $n = 3$ applies throughout the upper 410 km for free-slip models, and is restricted to $100 \text{ km} \leq z \leq 410 \text{ km}$ for prescribed plate-velocity models in order to improve numerical convergence.

Table 2. Radial viscosity structure η_r of the reference model.

layer number	depth [km]	viscosity [10^{21} Pa s]
1	0–100	50
2	100–300	0.1
3	300–410	0.1
4	410–660	1
5	660–2871	50

Here, z is depth, and z_c the depth of the CMB. The MM–NNR reference frame is established by removing the NR velocities that correspond to $\bar{\omega}$ from the numerical solution. NR flow given by $\bar{\omega}$ corresponds to an unconstrained motion of the whole mantle, which is physically allowed. Numerically, the velocities that correspond to the excited $\bar{\omega}$ are small, with rms values always $\lesssim 0.3 \text{ cm yr}^{-1}$.

2.2 Mantle rheology

The reference rheological model, η_r , is a generic profile (Hager & Clayton 1989, my table 2). This profile is broadly consistent with a range of studies and leads to azimuthal anisotropy model fits almost as good as those of more complicated profiles (Becker *et al.* 2003). I consider η_r as a simple reference for the radial viscosity structure of the mantle. For deviations from the layered viscosity, I test two rheologies. Firstly, a simplified law (A) (e.g. Christensen 1984):

$$\eta = \eta_r B(z) \dot{\epsilon}_{II}^{\frac{1-n}{n}} \exp \left[\frac{E}{n} (T_c - T) \right] \quad (2)$$

is used to study the individual effects of strain rate and temperature dependence (*cf.* Table 1). Here, $\dot{\epsilon}_{II}$ is the second (shear) strain-rate tensor invariant, E determines the strength of the temperature-dependence, and n is the power-law exponent. To isolate the effects of introducing different types of rheologies, $B(z)$ is adjusted for each layer of Table 2 and rheological models 1–4 of Table 3 such that the mean layer viscosity for LVVs is within 3 per cent of η_r (i.e. $B(z)$ is unity for all depths for the η_r case). Logarithmic averaging is used for η everywhere. By selecting the parameters as specified in Table 3, the role of power-law flow, temperature-dependent viscosity, and power-law and temperature-dependent viscosity in the upper mantle can be studied.

In the Earth's mantle, several deformation mechanisms will be active (Ashby & Verrall 1977), and at least a mixed rheology with diffusion and dislocation creep should be considered (*cf.* Ranalli 1995). I therefore, secondly, employ a joint diffusion/dislocation

creep law for the upper mantle which is based on the compilation of laboratory results for olivine deformation by Hirth & Kohlstedt (2004), as used, for example, by Billen & Hirth (2005). An effective viscosity (law B)

$$\dot{\epsilon}_{\text{total}} = \dot{\epsilon}_{\text{disl}} + \dot{\epsilon}_{\text{diff}} \quad (3)$$

$$\eta_{\text{eff}} = \frac{\eta_{\text{disl}}\eta_{\text{diff}}}{\eta_{\text{disl}} + \eta_{\text{diff}}} \quad (4)$$

is computed based on diffusion and dislocation creep viscosities (η_{diff} and η_{disl} , respectively). A general, laboratory derived creep law at constant water and melt content for these viscosities can be written as

$$\eta = \left(\frac{d^m}{A'}\right)^{\frac{1}{n}} \dot{\epsilon}_{II}^{\frac{1-n}{n}} \exp\left(\frac{E^* + pV^*}{nRT_r(T_c + T)}\right), \quad (5)$$

with parameters as given in Table 3. Here, d denotes grain size, m grain-size exponent, E^* and V^* activation energy and volume, respectively, T_r absolute reference temperature, and R the gas constant. A' is a constant that incorporates water and melt content and a conversion of laboratory creep laws for uniaxial straining under a differential stress to a regular viscosity law in SI units (see Appendix). Viscosity laws (2) and (5) can be related. If we choose the pre-exponential factors of both viscosities such that they yield the same value at reference conditions $p = 0$, $n = 1$, $T = T_c$, the temperature-dependence is equal for $T_c = 1$ if $E = E^*/(4RT_r)$. Rheology (5) needs further thermodynamic properties. To estimate pressure, p , in the upper mantle, I use an approximate relationship based on PREM (Dziewoński & Anderson 1981)

$$p(z) \approx 10^5 + 3.0429 \cdot 10^7 z + 7.687 \cdot 10^3 z^2,$$

where p is in Pa, and z in km. The pressure increase with depth is moderated in nature by an adiabatic temperature increase. The reference temperature T_r is set to 1583°K within the lithosphere and increases by 0.5°K km⁻¹ for depths below 100 km in the upper mantle. Within the lithosphere, a roughly error-function type of dependence is incorporated by the tectonic T model as described above (Fig. 1).

Seismic anisotropy is predominantly found in the boundary layers of the mantle (e.g. Montagner 1998). A common explanation for this is that lattice preferred orientation (LPO) anisotropy of olivine forms under dislocation creep, and that this mechanism should be dominant at relatively shallow (high-stress, low temperature) depths (e.g. Karato 1998; Hirth & Kohlstedt 2004). However, seismic anisotropy studies can, at present, not put firm constraints on the depth extent of dislocation creep (e.g. Trampert & van Heijst 2002; Wookey & Kendall 2004). I shall nonetheless proceed to focus on the role of power-law behaviour for the uppermost mantle for simplicity. Power-law creep is thus restricted to the upper 410 km for law A (see Table 3), or to the upper mantle as governed by the joint rheology (law B). Law B is certainly closer than law A to what we would expect from laboratory measurements for upper mantle olivine rheology. However, it is not clear which parameters (e.g. d , V^* , water content) apply for nature. Often the creep law parameters are, therefore, treated as adjustable to tune the transition between dislocation and diffusion dominated flow (e.g. McNamara & Zhong 2004). I have done the same here and will mostly discuss results for law B using dry olivine parameters as detailed in the Appendix.

In the case of the free-slip models, I additionally reduce the regular viscosity in the upper 100 km within 100 km distance from NUVEL-1 plate boundaries by a factor of 100 to allow for plate-like motion (Zhong *et al.* 2000). Particularly for the T -dependent

viscosity models, this is needed to not be in an entirely stagnant-lid regime at low temperatures. Details of the weak-zone formulation will be important for the magnitudes of plate velocities (King & Hager 1990; King *et al.* 1992; Yoshida *et al.* 2001), but I am not concerned with exact model predictions here. For all rheologies, η is restricted to only vary from 10¹⁷ to 10²⁴ Pa s for numerical stability. In the case of the upper-end truncation, this procedure may be considered as a rough approximation of plastic yielding at low temperatures close to the surface (Goetze & Evans 1979). I have conducted a few tests for different viscosity cut-off ranges, main conclusions presented here are not dependent on this choice.

2.3 Numerical approach

The Stokes equations in the Boussinesq approximation are solved for instantaneous circulation with the spherical finite element (FE) code `CitcomS` (Zhong *et al.* 2000) from `geoframework.org`; the original, Cartesian version was developed by Moresi & Solomatov (1995). `CitcomS` is well benchmarked and the implemented multi-grid solver is capable of treating LVVs at high resolution. For most computations, I use 196 608 elements laterally (~25 km element width at the surface), and 129 elements radially. The vertical spacing of elements is ~10 km in the upper mantle above 660 km and ~35 km below. All model velocities were interpolated on 1° × 1° grids in 44 layers for further visualization and analysis. With a lower resolution at a quarter of the number of elements, I was able to reproduce η_r Hager & O'Connell (1981) solutions with ~2 per cent rms velocity differences. Increasing the resolution to the full number of elements which is used here led to changes in velocities of a few percent for power-law computations, and I expect further refinement to lead to insignificant modifications.

For power-law viscosities, I iterate the FE velocity solution until the rms of the incremental change in velocities is below 1 per cent of the rms of the total velocity field. It was beneficial in some cases to perform this iteration in a damped fashion, using only a fraction (~0.75) of the new solution with updated viscosities for the next iteration step. For prescribed plate velocities with large strain rates across plate boundaries, it was not possible to reduce this mean difference between incremental velocity solutions during power-law loops to below ~3 per cent. I, therefore, only report results for prescribed velocity models where the lithosphere ($z < 100$ km) remains Newtonian. However, the velocities for full power-law computations are very similar to those shown here. The NR component for prescribed velocity models is somewhat sensitive to the choices as to the power-law iteration, and was observed to typically increase by ~15 per cent between 3 and 1 per cent rms velocity changes.

3 RESULTS AND DISCUSSION

First, example maps of velocities for different rheological models are presented. I then show both models with prescribed surface velocities and for free-slip; results are similar, indicating that model assumptions are dynamically consistent. Second, a quantitative analysis of similarities and differences between the rheological and flow character of the models is performed. This leads to a discussion of toroidal flow, and of net rotations of the lithosphere in particular. I conclude by commenting on implications for fitting observed plate motions.

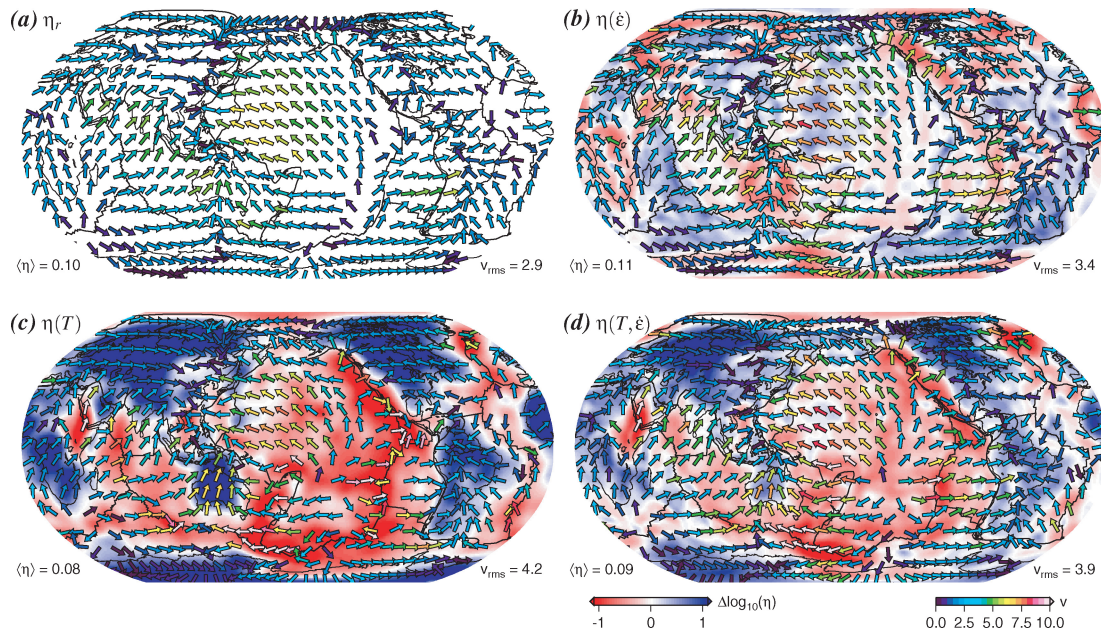


Figure 2. Flow velocities (fixed length vectors, amplitudes given by right colour bar and layer rms by lower right label, respectively, units of cm yr^{-1}) and viscosity variation from the layer mean ($\log_{10}(\eta) - \langle \log_{10}(\eta) \rangle$), where $\langle \rangle$ indicates the average, as specified on lower left of figures, units of 10^{21} Pa s) at a depth of 250 km for plate-motion prescribed models. Velocities are given in the mean mantle NNR reference frame. Plots (a), (b), (c), and (d) show results for the radial reference model, η_r , pure power law, $\eta(\dot{\epsilon})$, T -dependent viscosity, $\eta(T)$, and for power law plus T -dependence, $\eta(T, \dot{\epsilon})$, model, respectively (see Table 3). Compare with Fig. 3 for free-slip models.

3.1 Velocity maps

Fig. 2 shows velocities and LVVs with respect to the layer mean for the velocity-prescribed models for the four rheological set-ups 1–4 of Table 3. I show flow in the MM–NNR reference frame at a depth of 250 km. Comparison of reference model a) with the pure power-law computation (Fig. 2b) shows that strain-rate dependent creep alone does not modify the circulation pattern substantially, though it does lead to larger velocity amplitudes in regions such as the NW Pacific. Following the distribution of induced strain rates, the viscosity is decreased underneath some oceanic plates, and particularly underneath a few continental regions such as western North America and central Europe. Such LVVs and corresponding differences in velocities are found at the boundaries of the compositionally distinct regions (*cf.* Fig. 1). The relatively stagnant keels lead to regions of weakened viscosity around them. This effect is absent in models that have no lateral compositional differences; pure power-law flow for these models is then very similar to the reference model, with slight weakening of average viscosity underneath oceanic plates. The finding that pure power-law flow is similar to Newtonian flow is consistent with early findings for 2-D thermal convection (Parmentier 1978; Christensen 1984), and with Čadek *et al.*'s (1993) study. It is also not too surprising given the fairly smooth lateral density variations as inferred from global tomography or my tectonic model. Comparison of Figs 2(a) and (c) shows that temperature-dependent viscosity does lead to some rearrangement in flow patterns, most pronounced underneath oceanic plates where tomographic anomalies are mapped into LVVs. Correspondingly, velocity directions are different, for example, for $\eta(T)$ in the super-swell region in the southwest Pacific, and within a channel that roughly parallels the East Pacific Rise (EPR) at a distance of ~ 1250 km to the west. Flow patterns close to this anomalous channel have been discussed by Gaboret *et al.* (2003) in the context of

seismic anisotropy for a η_r -type flow model. Further analysis (not shown) reveals other regions where flow is affected by temperature-dependent viscosity: underneath the ridges themselves and in areas with fast, presumably subduction-related, tomographic anomalies ('slabs'), such as under central North America. Such modifications in flow are caused both by the stirring action of strong continental roots (Zhong 2001; Čadek & Fleitout 2003) and by the relatively weak material underneath oceanic plates.

The $\eta(T)$ model also differs from η_r flow in terms of the velocity amplitudes. At 250 km depth $\eta(T)$ shows larger velocities on average, with global rms (maximum) values increased from 2.9 (6.8) (Fig. 2a) to 4.2 (33.2) cm yr^{-1} (Fig. 2c). Velocities for LVV flow are enhanced by up to a factor of ~ 30 underneath the channel anomaly, and by factors of ~ 10 underneath some of the ridges. Adding power-law creep to the temperature-dependent viscosity (Fig. 2d) reduces the LVVs. This is expected from the reduced effective temperature-dependence, E/n in eq. (2), and the regulating effects as seen in thermal convection models (Christensen 1984). Accordingly, rms and maximum velocities at 250 km depth are reduced to 3.9 and 25.1 cm yr^{-1} , respectively, for $\eta(T, \dot{\epsilon})$. The geographic distribution of deviations in terms of velocity patterns is different between the $\eta(T, \dot{\epsilon})$ and $\eta(T)$ model. Adding strain-rate weakening tends to emphasize the velocity discrepancies in regions of upwellings such as the East African Rift and the channel anomaly. However, flow around slabs appears more similar to η_r for $\eta(T, \dot{\epsilon})$ than for $\eta(T)$, as the relative strength contrast of the cold anomalies is lower for models that incorporate strain-rate dependent viscosities.

Surface wave tomography clearly images half-space cooling structure underneath oceanic plates up to depths of ~ 150 km (e.g. Ritzwoller *et al.* 2004). This is expected from the common geodynamic point of view where mostly passive spreading at the ridges transitions to cooling of oceanic plates toward the trenches. Somewhat unexpected is that slow v_s is commonly found

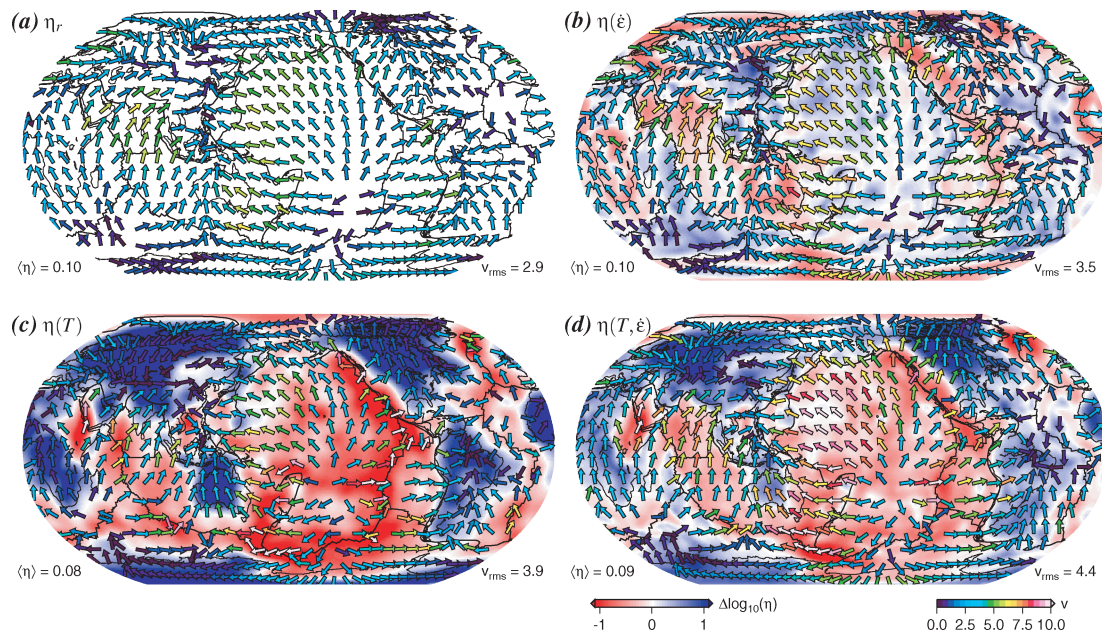


Figure 3. Velocities and viscosity variation at 250 km for free-slip convection models with different rheological set-ups, for description see Fig. 2.

underneath major ridges up to depths of ~ 300 km (e.g. Becker & Boschi 2002). Correspondingly, my models exhibit a broad, low viscosity ‘asthenosphere’ underneath the ridges, as $\eta(T)$ depends on the scaled $d \ln v_S$ -anomalies. To test the importance of sub-oceanic anomalies within the upper 300 km, I also computed flow for $\eta(T, \dot{\epsilon})$ models where no tomographic structure was used for the upper 300 km anywhere. Only half-space cooling and stiff continental roots were imposed, which in itself leads to relatively low viscosity underneath the oceanic plates (Čadek & Fleitout 2003). The large-scale flow patterns of such a simplified LVV model are similar to what is shown in Fig. 2(d). The stirring action of the prescribed continental roots is, however, more pronounced, as there are few other anomalies in the shallowest mantle. Consequently, large differences between η_r and $\eta(T, \dot{\epsilon})$ flow are found close to the roots. The channel anomaly east of the EPR persists, indicating that buoyancy sources deeper than ~ 300 km are important for this pattern. Average velocity amplitudes at 250 km are reduced to 3.5 from 3.9 cm yr^{-1} in Fig. 2(c), and the maximum velocities are only 10.4 cm yr^{-1} without the shallow anomalies.

Are the velocity results and rheology consistent with regard to driving forces, or are they artefacts induced by the prescribed plate motions? Fig. 3 shows velocities at 250 km for the same rheological and density set-ups but free-slip/weak-zone surface boundary conditions. The general flow patterns of Fig. 3 match those of Fig. 2 well. This is not surprising, as we know that global circulation models are able to predict plate motions (e.g. Ricard & Vigny 1989; Lithgow-Bertelloni & Richards 1998; Zhong 2001). However, the match is reassuring, and also the general behaviour of flow modification as a function of rheology is similar for the free-slip and prescribed plate-motion models. The rms and maximum velocities at 250 km depth are 2.9 (6.8), 3.9 (34.6) and 4.4 (19.8) cm yr^{-1} for the reference, $\eta(T)$, and $\eta(T, \dot{\epsilon})$ model, respectively. Below, the fit to present-day plate motions is discussed further.

In terms of rheology, there are no significant global differences we can distinguish visually between Figs 2 and 3. This implies that the prescribed surface velocities of Fig. 2 do not unduly constrain the large-scale variations in strain rate compared to freely deform-

ing models. The geographic regions where $\eta(T)$ and $\eta(T, \dot{\epsilon})$ models show strongly different velocities from η_r flow are more confined for the free-slip models than for the prescribed velocity approach. In terms of orientations, the deviations are more focused underneath ridges and much reduced underneath central North America as well as around slab regions. While the channel anomaly is still a strong feature for different rheological models for free-slip, it is more focused toward the SW of the EPR. These regional differences between Figs 2 and 3 imply that in those locations, the purely buoyancy-driven flow does not closely match the velocities of the prescribed velocity approach. The situation in nature will likely fall somewhere in between my simplified end-member cases.

3.2 Average viscosity profiles

Fig. 4 shows the depth dependence of the logarithmic mean of the of viscosity and its rms variation for models with $\eta(T)$, $\eta(T, \dot{\epsilon})$ and η_{eff} rheologies (Table 3). These averages were calculated for free-slip circulation as shown in Figs 3(c) and (d). However, the corresponding results for the prescribed velocity computations are very similar. My particular choice of temperature-dependence ($E = 30$ for model $\eta(T)$) leads to viscosity variations up to ~ 1.5 orders of magnitude in terms of rms variations (Fig. 4a). The maximum variability is found in the upper boundary layer at ~ 150 km, as expected from the variation of tomographic anomaly strength with depth (e.g. Becker & Boschi 2002) and thermal convection computations (e.g. Zhong *et al.* 2000). When the mean viscosity is computed underneath oceanic and continental regions separately, a \sim one order of magnitude difference is predicted for purely T -dependent viscosity between 100 km and 410 km depth. Even though the average for the 0–100 km layer for $\eta(T)$ is made to match the η_r value of $5 \cdot 10^{22}$ Pa s, the mean surface viscosity is $\sim 5 \cdot 10^{23}$ Pa s which implies relatively sluggish surface motions.

So far, no flow computation would have been necessary for these statements about $\eta(T)$ viscosities. However, the evaluation of consistent strain rates becomes important for power-law computations

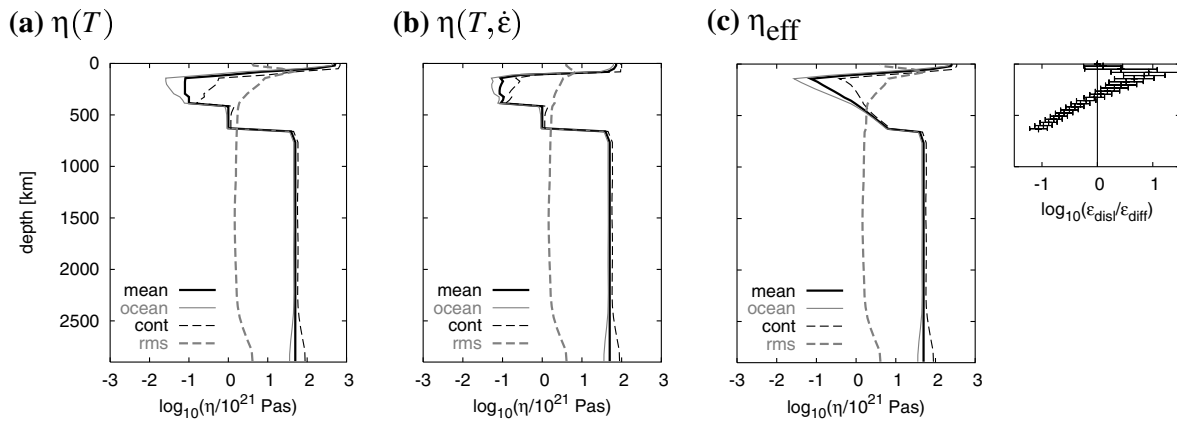


Figure 4. Depth dependence of log-averaged viscosity and rms deviations for rheological models $\eta(T)$ (a), $\eta(T, \dot{\epsilon})$ (b), and η_{eff} (c) for the free-slip models of Fig. 3. Black solid lines indicate the mean (constrained to match η_r to within 3 per cent for models a and b), and grey-solid and dashed-black lines denote the mean underneath oceanic and continental regions (from 3SMAC), respectively. The dashed-grey line indicates the rms variations of $\log_{10}(\eta)$. For the joint diffusion/dislocation creep rheology of the η_{eff} model (c), I also show the mean \pm rms of the strain-rate partitioning (see eqs 4 and 6).

(Figs 4b and c). The regional discrepancy of viscosity averages underneath oceanic and continental plates, and the total η variability, are reduced by the introduction of power-law flow, as mentioned for the 250 km depth layer example above. A factor ~ 5 difference between average η underneath oceanic and continental plates is found for $\eta(T, \dot{\epsilon})$, suboceanic viscosities are weaker by ~ 3 if we remove the anomalies inferred from tomography above 300 km. Surface viscosities for $\eta(T, \dot{\epsilon})$ are smaller than for $\eta(T)$, as the power-law dependence weakens the thermally-induced high viscosity lid.

The reduction of variability in η due to introduction of strain-rate weakening becomes important if we wish to evaluate mantle tractions for plate coupling models (Čadek & Fleitout 2003), as those tractions scale with the viscosity contrasts (Conrad & Lithgow-Bertelloni 2006). Given the results shown in Figs 2–4, it appears feasible to derive an effective T -dependent rheology with reduced temperature dependence $E' \sim E/n$, whose tractions and viscosity variations match those of a more complete, $\eta(T, \dot{\epsilon})$, rheology. Such a rescaling was detailed by Christensen (1984) for 2-D convection, but the establishment of a quantitative relationship is outside the scope of this paper.

Models $\eta(T)$ and $\eta(T, \dot{\epsilon})$ were constructed to isolate the effects of $\dot{\epsilon}$ and T on viscosity, and were constrained to match the radial average η_r . As a check, Fig. 4(c) shows results for the joint dislocation/diffusion creep rheology, η_{eff} , that is based on olivine creep laws. For the choice of laboratory-derived parameters in Table 3, it is possible to obtain a depth-averaged viscosity structure that roughly resembles η_r , both for the prescribed surface velocity and the free-slip models. The offset of the suboceanic and continental viscosity averages is confirmed for this model. While mostly a direct consequence of my input model choices (e.g. strong continental roots up to 300 km), it is interesting that all models are consistently producing an oceanic asthenosphere that is \sim one order of magnitude weaker than the subcontinental regions in the transition zone (cf. Čadek & Fleitout 2003).

Taking the compilation of Hirth & Kohlstedt (2004) at face value for rock behaviour in the upper mantle, I found that wet parameters led to average viscosities that were about a factor of ~ 50 lower than those of η_r between ~ 150 and 500 km. Minimum $\langle \eta \rangle$ viscosities at ~ 200 km depth are $4.4 \cdot 10^{18}$ and $1.4 \cdot 10^{18}$ Pa s for water contents of $C_{OH} = 100$ and 1000 H/10⁶Si, respectively (see Appendix), com-

pared to $8.9 \cdot 10^{19}$ Pa s for η_{eff} as shown. The better match between average viscosities is why I used dry values for A' and creep law parameters. For the η_{eff} model with free-slip boundary condition and weak zones as shown in Fig. 4(c), log-averaged $\dot{\epsilon}_{II}$ values for the four upper mantle layers of Table 2 are $\approx 2, 42, 19$, and $8 \cdot 10^{-16} \text{ s}^{-1}$, and $2 \cdot 10^{-16} \text{ s}^{-1}$ for the lower mantle. For the prescribed surface velocity η_{eff} model, all $\dot{\epsilon}_{II}$ averages are similar to the free-slip case, but the top 100 km average is only $1 \cdot 10^{-16} \text{ s}^{-1}$.

I measure the partitioning between dislocation and diffusion creep by

$$\gamma = \log_{10}(\dot{\epsilon}_{\text{disl}}/\dot{\epsilon}_{\text{diff}}), \quad (6)$$

meaning that $\gamma \gg 0$ corresponds to dislocation-creep dominated deformation, and vice versa. The average $\langle \gamma \rangle$ and its rms variations in the upper mantle are shown in the subplot of Fig. 4(c) for the η_{eff} model. For the modelling choices of Table 3, γ crosses zero at ~ 300 km depth. This transition depth and the general shape of $\langle \gamma \rangle$ for the joint rheology are broadly consistent with LPO dominated seismic anisotropy in the uppermost mantle forming under dislocation creep (cf. Podolefsky *et al.* 2004). At depths which are predominantly in the dislocation creep regime, for example, at 200 km, the cold, stiff continental roots as well as regions around slabs show the largest γ , consistent with results by McNamara *et al.* (2003). At the same depths, some oceanic regions close to ridges are predicted to be in the diffusion creep regime with $\gamma < 0$. Details in the dependence of $\langle \gamma \rangle$ on depth such as the zero-crossing (i.e. the average transition stress between dislocation and diffusion creep) depend strongly on the creep law parameters such as d . However, the overall shape of $\langle \gamma \rangle$ and regional patterns in γ are more robust with regard to parameter choices. The spatial distribution of γ are of interest for the study of LPO development.

The results with regard to the effective viscosity creep-law are dependent on the rheological parameters, which are not particularly well constrained, even for the upper mantle. However, the main point here is that it is possible to construct a dynamically plausible flow model, like my η_{eff} case. This set-up is broadly consistent with canonical radial viscosity averages such as η_r , with laboratory findings on rheology, and with the present understanding of LPO anisotropy.

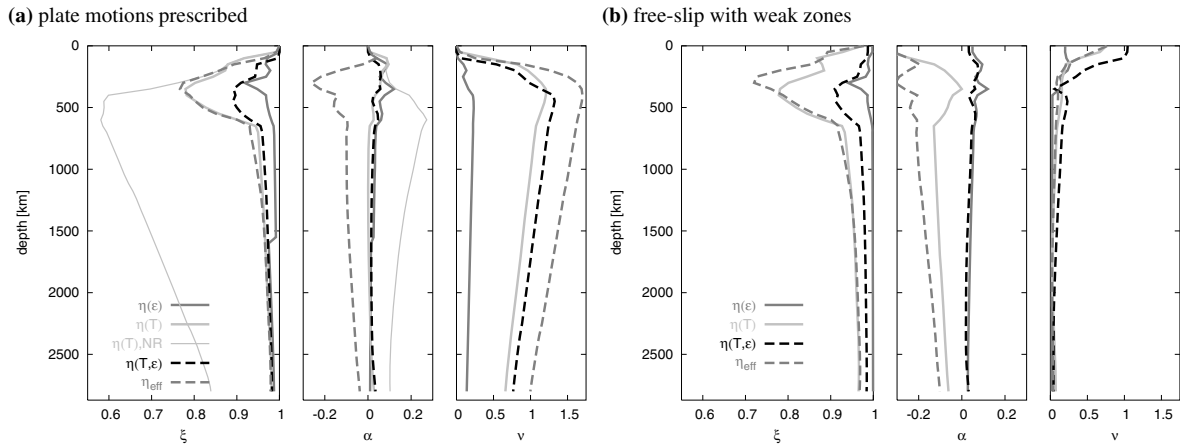


Figure 5. Depth dependence of the mean, velocity-weighted dot product of normalized velocities ($\xi = \langle \mathbf{v}^n \cdot \mathbf{v}_r^n \rangle_{|\mathbf{v}|/|\mathbf{v}_r|}$, left), mean of the logarithmic velocity amplitude ratio ($\alpha = \langle \log_{10}(|\mathbf{v}|/|\mathbf{v}_r|) \rangle$, centre), and NR amplitude as a fraction of GJ86 of each velocity layer (v , right subplots) for different rheological models \mathbf{v} (see Table 3). All comparisons use the η_r model as the reference (\mathbf{v}_r). Figure (a) compares velocities for models where plate velocities were prescribed at the surface in a NNR reference frame. However, any layer NR was removed before computing ξ or α for all cases but ‘ $\eta(T)$ NR’, which compares the full $\eta(T)$ and η_r velocities. Plot (b) compares free-slip, weak zone models in a consistent, mean mantle MM–NNR reference frame.

3.3 Quantitative comparison of velocity fields

Fig. 5 shows global velocity variations as a function of rheology and depth. I compute a correlation-like measure

$$\xi = \langle \mathbf{v}^n \cdot \mathbf{v}_r^n \rangle_{|\mathbf{v}|/|\mathbf{v}_r|} \quad (7)$$

from a weighted average of the dot product of the normalized test (LVV) and reference (η_r) model velocities, $\mathbf{v}^n = \mathbf{v}/|\mathbf{v}|$ and $\mathbf{v}_r^n = \mathbf{v}_r/|\mathbf{v}_r|$, respectively, where $|\cdot|$ denotes the vector norm. The global mean is weighted by the product of the local velocity amplitudes of the fields to give more weight to regions that exhibit stronger flow. (ξ is typically larger by ≈ 0.05 than an unweighted mean correlation $\langle \mathbf{v}^n \cdot \mathbf{v}_r^n \rangle$.) For analysis of amplitude changes, a mean logarithmic amplitude ratio referenced to η_r , is used

$$\alpha = \langle \log_{10}(|\mathbf{v}|/|\mathbf{v}_r|) \rangle. \quad (8)$$

Fig. 5 also shows the NR component of the velocities at each depth, normalized by the amplitude of NR in the GJ86 hotspot reference

Table 4. NR Euler vectors, $\omega(0)$, of the lithosphere as inferred from hotspot reference models and numerical computations (free-slip in the mean-mantle NNR reference frame). Model labels refer to those used in Fig. 6.

Model label	Reference	Longitude	Latitude	Amplitude [$^\circ \text{ Myr}^{-1}$]
Plate reconstruction models				
GJ86	Gordon & Jurdy (1986)	37°E	40°S	0.115
T22	Wang & Wang (2001)	88°E	62°S	0.142
HS3	Gripp & Gordon (2002)	70°E	56°S	0.436
SB04 ^a	Steinberger <i>et al.</i> (2004)	38°E	40°S	0.165
Geodynamic free-slip computations				
Z01	case 4 of Zhong (2001)	103°E	42°S	0.092
$\eta(\dot{\epsilon})$		33°E	33°N	0.023
$\eta(T)$		97°E	54°S	0.087
$\eta(T, \dot{\epsilon})$		71°E	46°S	0.114
η_{eff}		94°E	45°S	0.088

Note: ^aThe SB04 pole is an updated hotspot reference frame estimate using the procedure of Steinberger *et al.* (2004) (B. Steinberger, personal communication, 2006).

model by Gordon & Jurdy (1986) (see Table 4):

$$v = \frac{|\omega|}{|\omega_{\text{GJ86}}(0)|}. \quad (9)$$

Fig. 5(a) shows how velocity solutions vary from those of the reference model, η_r , for model rheologies 2–5. A substantial NR component of flow is introduced by all models with LVVs. This is particularly evident for models with T -dependent viscosity. For such cases, the NR reaches ~ 1 – 1.5 the GJ86 hotspot reference-frame values at ~ 400 km depth, even though the surface velocities were constrained to be in the NNR reference frame. This implies that NNR plate motions are physically incompatible with the rheological models. If these NR components of flow are not accounted for, velocity predictions for LVV models can be quite different from those for η_r models at depths larger than ~ 400 km. This can be seen by the comparing ξ for velocities from the original $\eta(T)$ solution (thin grey line) with ξ for velocities which had any NR component at each layer removed (all other graphs in the left portion of Fig. 5a). I return to the question of reference frames below. Here, all other ξ and α measures for the plate-driven models in Fig. 5(a) are computed after a layer-based NR correction is applied: At each depth level, the NR is computed and subtracted from the velocities. Conversely, Fig. 5(b) uses a consistent MM–NNR reference frame.

Comparing ξ for the different rheological models in Fig. 5(a), I find that pure power-law flow models are indeed very similar at $\xi \gtrsim 0.92$ at all depths, as expected. Introducing T -dependent η reduces the correlation to minimum values of $\xi \sim 0.75$. Such deviations in velocity fields are comparable to other uncertainties, such as those due to our incomplete knowledge about the temperature structure of the mantle. As anticipated above, the joint $\eta(T, \dot{\epsilon})$ model leads to smaller deviations from η_r (black dashed line in Fig. 5a). For the particular choices of Table 3, the effective viscosity model leads to variations in velocities that are similar to the $\eta(T)$ case. Mean variations in amplitude of flow are quite small (mid plot of Fig. 5a) and for the η_{eff} model at ~ 400 km. The η_{eff} case is the only one where average layer viscosities were not formally constrained to match η_r , so this comparison is somewhat misleading. Most changes in amplitude α for $\eta(T)$ and $\eta(T, \dot{\epsilon})$ are due to faster flow underneath the oceanic plates (*cf.* Fig. 2). The ξ and α values in Fig. 5(a) imply

that the gross structure of flow will be similar for different rheological model predictions. However, regionally, deviations such as in the SW Pacific (*cf.* Figs 2 and 3) may be important. Using regional predictions and constraints such as from seismic anisotropy may in fact allow to put further bounds on the rheology of the mantle.

The details of the depth dependence of the quantities computed for Fig. 5 depend on η_r , and in particular the low viscosity channel from 100 to 410 km (Table 2). However, I also computed velocities for a simpler η_r viscosity with only three layers ($\eta_r(100 \text{ km} \leq z \leq 660 \text{ km}) = 10^{21} \text{ Pa s}$). Results are broadly consistent with, but expectedly smoother than, those presented in Fig. 5. The amplitudes and the trend among different rheological models for ξ is preserved for the simpler η_r . Amplitude ratio variations are closer to zero than for the η_r used for Fig. 5, with slight $\alpha < 0$ velocity reduction in the upper mantle for laterally varying viscosity models. I also tested *ngrand* (Grand 2001) as an alternative seismic tomography model to infer temperature. Results are again similar to what is shown in Fig. 5(a), with larger rms viscosity variations for $\eta(T)$ models than for *smean*. Such behaviour is expected given that *ngrand* has more power at higher spatial frequencies than *smean* (Becker & Boschi 2002). While trends between different rheological models are preserved, minimum ξ values are reduced by ~ 0.1 compared to Fig. 5(a) for *ngrand*.

Fig. 5(b) repeats the comparison among rheological models for the respective free-slip computations. Velocities were transformed into the MM–NNR reference frame. The general findings as to the different degrees of similarity for rheological models as expressed by ξ are confirmed for these self-consistent models. Congruent with Conrad & Lithgow-Bertelloni (2006) study, my results indicate that the variations in the directions of flow, and hence tractions, are moderate when more realistic rheologies are incorporated in mantle flow models. Correlation values are always $\xi \gtrsim 0.8$ in the uppermost mantle ($z \gtrsim 200 \text{ km}$), and do not drop below $\xi \sim 0.7$ when they are least similar at $\sim 400 \text{ km}$ depth. Amplitude variations with depth among different free-slip models are moderate for all but the $\eta(T)$ and η_{eff} models in Fig. 5(b). The relatively slow velocities for these strongly temperature-dependent cases are caused by the large surface viscosities mentioned above. Introducing strain-rate weakening rheologies allows the plates to move more freely for $\eta(T, \dot{\epsilon})$ (*cf.* Solomatov & Moresi 1997; Zhong *et al.* 1998), but also leads to a loss of flatness in my large-scale flow models, as discussed below.

3.4 Generation of net lithospheric motion by stiff continental roots

3.4.1 Net surface rotation

For free-slip models, the choice of velocity reference frame is arbitrary (Zhong 2001). However, the mean mantle NNR reference frame is appealing, and makes it easier to study the generation of net motion. The right subplot of Fig. 5(b) shows that all models with LVVs excite a NR component of flow which is focused in the upper $\sim 400 \text{ km}$. A very similar depth dependence was documented by ZH01. The NR component of the η_r free-slip model should be exactly zero from theory, and is always $v < 0.1$ per cent when computed numerically. This number provides a bound on the accuracy of the FE method and the velocity analysis procedure. For my free-slip models with LVVs in the MM–NNR frame, the lithosphere moves with regard to a relatively stable lower mantle with a sense that is con-

sistent with hotspot reference frames such as HS3 (Table 4). Zhang & Christensen (1993), Čadek *et al.* (1993) and Wen & Anderson (1997) previously studied the excitation of NR in global, spherical models. These studies, however, found that neither amplitudes, nor directions of NR motion were matched well compared to a hotspot reference. One reason for this may be that very little toroidal motion, such as NR flow, is excited for purely temperature-dependent LVVs (Christensen & Harder 1991; Ogawa *et al.* 1991). Bercovici *et al.* (2000) suggest that in order to efficiently generate toroidal flow, it is necessary that buoyancy and viscosity anomalies are spatially out of phase. Such conditions are given for the case of weak zones at plate boundaries (e.g. Zhong *et al.* 1998) or non-linear, strain-weakening rheologies (Bercovici 1995; Tackley 2001b).

More recently, Zhong (2001) showed that strong continental roots and weak zones can indeed generate NR motion of the lithosphere, and my findings are consistent with his results. ZH01 varied the depth of the roots to analyse their effect on the generation mechanism and found that the deepest continental roots that were considered (down to 410 km depth) were able to generate the largest NR motion, $v \approx 80$ per cent. Table 4 provides an overview of published estimates of net lithospheric rotation in hotspot reference frames; Euler pole locations are plotted in Fig. 6. The exact nature of the observed net motion of the present-day plates with regard to hotspots is debated and intimately related to the question of hotspot-fixity with respect to the lower mantle. If motions of hotspots are accounted for (Steinberger *et al.* 2004), amplitudes of NR are reduced compared to the HS3 model, but still larger than GJ86 (Table 4). I, therefore, compare previous and my modelling results for net rotations with a range of published models (Fig. 6).

Using the general geodynamic model set-up, I find that strain-rate dependence with $n = 3$ and weak zones alone are ineffective in introducing NR motion (*cf.* Čadek *et al.* 1993; Bercovici 1995); rotation poles are far from published hotspot estimates (Fig. 6). However, when temperature-dependent viscosities are introduced on top of the weak-zone formulation, the pole moves closer to estimates such as

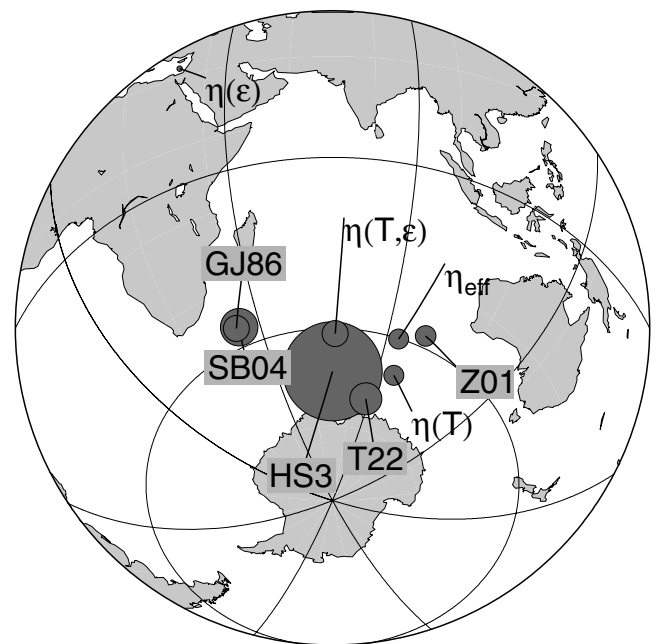


Figure 6. Location and magnitude (circle radius) of NR Euler poles from several hotspot reference models and my geodynamic computations, labels and values given in Table 4.

HS3 (Fig. 6). Amplitudes reach 76 per cent of the GJ86 estimates, or 20 per cent of HS3 for $\eta(T)$. This finding substantiates results by ZH01, at somewhat reduced continental root depths compared to that study. Interestingly, the power-law rheology of $\eta(T, \dot{\epsilon})$ enhances the NR component, up to 99 per cent of GJ86 or 26 per cent of HS3. The predicted Euler pole locations of my free-slip models are given in Table 4 and Fig. 6 and match those of HS3 closely. It seems that the rheologies employed in this study lead to somewhat larger NR amplitudes than those used in ZH01.

3.4.2 Toroidal:poloidal partitioning

The enhanced generation of net motions is related to the more effective generation of toroidal flow by $\eta(T, \dot{\epsilon})$ models. One common diagnostic measure is the ratio between toroidal and poloidal velocity fields at the surface (O’Connell *et al.* 1991; Tackley 2001a). I compute the toroidal:poloidal ratio Θ_i as

$$\Theta_i = \frac{p_i^{p,t}}{p_i^p}, \quad (10)$$

where $p_i^{p,t}$ is the total power of a spherical harmonic expansion of the velocity field components,

$$p_i^{p,t} = \frac{1}{2\sqrt{\pi}} \sqrt{\sum_{\ell=i}^{\ell_{\max}} \sum_{m=0}^{\ell} (a_{\ell m}^2|_{p,t} + b_{\ell m}^2|_{p,t})}. \quad (11)$$

Here, $\{a_{\ell m}, b_{\ell m}\}|_{p,t}$ are the real spherical harmonic coefficients of the poloidal (subscript p) or toroidal (subscript t) field (as defined in eqs. B.99 and B.158–160 of Dahlen & Tromp 1998), and I use $\ell_{\max} = 63$.

With definition eq. (10), Θ_1 includes the $\ell = 1$ NR component ν , and Θ_2 measures the toroidal:poloidal power partitioning without NR. Table 5 lists surface Θ and ν values for tectonic and geodynamic models; $\Theta_1 \sim 1$ for HS2 and HS3. The non-NR toroidal:poloidal partitioning is $\Theta_2 \sim 0.5$ for plate models such as NUVEL-1, and has been at similar levels in the convective past (Lithgow-Bertelloni *et al.* 1993). Since the surface ratio of toroidal to poloidal power has a white spectrum (O’Connell *et al.* 1991), details such as the

tapering of my spherical harmonic expansion of NUVEL-1 do not affect Θ_2 much (Dumoulin *et al.* 1998).

Table 5 compares surface velocity diagnostics for tectonic models and those computed from free-slip convection computations. The toroidal:poloidal ratio for η_r is $\Theta_{1,2} = 0.37$ which indicates the effect of the weak zones. The imposed plate geometry in itself generates toroidal motion and organizes the flow (Gable *et al.* 1991), in particular for motions on the surface of a sphere (O’Connell *et al.* 1991; Olson & Bercovici 1991). Introducing power-law rheology alone does not increase the toroidal power, as expected from Bercovici (1995) experiments. However, all LVV models with temperature-dependent viscosity have increased Θ_2 of 0.4–0.5. Those values are comparable to the toroidal power in NUVEL-1 (for $\ell \geq 2$, Table 5). The η_{eff} case shows Θ_2 toroidal power that is similar to NUVEL-1 values and larger than Θ_2 for $\eta(T, \dot{\epsilon})$. Since the NR of η_{eff} is smaller than that of $\eta(T, \dot{\epsilon})$, this means that surface velocities of η_{eff} are more Earth-like with regard to Θ partitioning, but absolute amplitudes of NR are slower than in hotspot reference frames. I expect NR Euler pole locations and toroidal:poloidal partitioning to be better measures of realism than exact values of NR, ν .

3.4.3 Generation of toroidal motion

Wen & Anderson (1997) showed that the introduction of rheological oceanic/continent differences excites toroidal flow by mode coupling in their low order spherical harmonics models. My models refine the results by Wen & Anderson, using what I consider a more consistent approach for arriving at differences in viscosity underneath different plate regions. My finding of increased Θ with LVVs is also in agreement with ZH01, where values of $\Theta_1 \sim 0.5$ were produced for the deepest continental root model, in analogy with the discussion of the excitation of net motion above. Tackley (2001b) studied how Θ_2 varies with depth and found enhanced generation of toroidal flow for some of his non-linear rheology cases. I have also analysed Θ_2 as a function of depth for the free-slip computations. All models with T -dependent LVVs show larger $\Theta_2(z)$ throughout

Table 5. Surface velocity diagnostics for tectonic and geodynamic free-slip models: Π : plateness (eq. 13), Ω : oceanic to continental rms speed ratio, $\xi(0)$: similarity of predicted surface velocities to NUVEL-1 plate motions (eq. 7), $\Theta_1(0)$, $\Theta_2(0)$: toroidal: poloidal power ratio with and without the NR component (eq. 10), and $\nu(0)$: NR normalized by GJ86 (eq. 9, see Table 4). (Parameters ξ , Θ_i and ν are evaluated at the surface.) Velocities from the free-slip, weak-zone models are computed in the MM–NNR frame, may include an NR component for the LVV cases, and should thus be compared with hotspot reference frame tectonic models. All models were sampled on $1^\circ \times 1^\circ$ grids. References: NUVEL-1 NNR: DeMets *et al.* (1990); NUVEL-1 HS2 Gripp & Gordon (1990); NUVEL-1A HS3: Gripp & Gordon (2002); GSRM–NNR: Kreemer *et al.* (2003).

Model	Plateness	oc/co speed ratio	Plate motion fit	Toroidal:poloidal power ratio		Net rotation
	Π	Ω	$\xi(0)$	with ν $\Theta_1(0)$	w/o ν $\Theta_2(0)$	$\nu(0)$
Tectonic models						
NUVEL-1 HS2	1	2.9	–	0.92	0.53	2.88
NUVEL-1A HS3	1	2.7	–	1.17	0.53	3.79
NUVEL-1 NNR	1	2.3	–	0.53	0.53	0
NUVEL-1 NNR, smoothed at $\ell_{\max} = 63$	0.87	2.3	–	0.52	0.52	0
GSRM–NNR ^a	0.87	2.1	–	0.57	0.57	0
Geodynamic free-slip models						
η_r	0.56	1.7	0.83	0.37	0.37	0
$\eta(\dot{\epsilon})$	0.55	1.7	0.83	0.37	0.37	0.20
$\eta(T)$	0.96	3.0	0.93	0.55	0.43	0.76
$\eta(T, \dot{\epsilon})$	0.51	2.5	0.90	0.42	0.38	0.99
η_{eff}	0.91	3.2	0.95	0.58	0.50	0.76

Note: ^aSince the GSRM–NNR model is not global, the polar regions were interpolated based on best-fit rigid plate motions for the Antarctic, North American and Eurasian plate.

the mantle than η_r or $\eta(\dot{\epsilon})$ cases. I find that the toroidal:poloidal partitioning decreases from the surface values of Table 5 for $\eta(T)$ to a minimum at ~ 2000 km depth. At greater depths, there is a slight increase toward the CMB. This behaviour indicates a scaling of Θ_2 with the strength of the LVVs as inferred from the $d \ln v_s$ anomalies of tomography (see also rms variations of η in Fig. 4). However, Θ_2 increases from $\Theta_2(0) \sim 0.4$ to a sublithospheric maximum of $\Theta_2 \sim 0.8$ at ~ 150 km for $\eta(\dot{\epsilon})$ and η_{eff} flow, before decreasing toward the lower mantle (*cf.* Tackley 2001b). This finding substantiates that non-linear rheologies play a role for toroidal flow generation, even in the presence of prescribed weak zones.

Given findings by Christensen & Harder (1991), Martinec *et al.* (1993) and Bercovici *et al.*'s (2000) suggestion that pure T -dependent convection will not be efficient in generating toroidal flow, I also computed $\Theta_2(z)$ for models similar to the $\eta(T)$ case but without compositional anomalies c in the continental keels. Results were very similar to $\eta(T)$ flow with compositional anomalies. If weak zones along plate boundaries are also omitted, $\Theta_2(0)$ drops to zero as there is almost no motion at the surface in this rigid lid case. However, Θ_2 does increase to ≈ 0.45 at ~ 250 km depth, and then follows the $\Theta_2(z)$ behaviour at depth as seen for $\eta(T)$ flow with weak zones. This finding indicates that purely temperature-dependent LVVs can generate significant toroidal motion in global circulation models where ‘temperature’ really means ‘scaled velocity anomalies’. I conjecture that thermal convection does not generate significant toroidal flow for purely temperature-dependent viscosity, but $\eta(T)$ type flow models do as they use information from tomography, which maps the thermo-chemical convective state of the Earth.

To evaluate the role of continental root rheology for the excitation of NR further, I conducted a series of tests with strain-rate and temperature-dependent rheology of type $\eta(T, \dot{\epsilon})$. The simplified tectonic model without any tomographic anomalies above 300 km is used in order to isolate the role of strong roots, whose strength is varied by increasing the non-dimensionalized activation energy. Fig. 7 shows how the ratio of mean cratonic or subcontinental to ambient viscosity between 100 and 250 km depth increases with the non-dimensional temperature-dependence E/n ($n = 3$, eq. 2). I show results for both prescribed plate motion and free-slip models (*cf.* v -plots in Fig. 5). For both mechanical boundary conditions, increasing E/n up to ~ 6 leads to a strong increase in the viscosity ratios of cratonic and continental regions, as expected. However, the strain-rate dependence of the $\eta(T, \dot{\epsilon})$ rheology then appears to limit a further increase in viscosity contrast, and cratons and continental regions are asymptotically stiffer by a factor of ~ 15 and ~ 5 , respectively. If this weakening effect of strain-rate dependent viscosity is confirmed with dynamical 3-D models, the effective viscosities of continental roots might not be large enough to sufficiently retard destabilization over geologic times (e.g. Lenardic & Moresi 1999).

Fig. 7 also shows how the NR of the lithosphere, ν , depends on LVVs. The NR increases with the mean viscosity ratios for both mechanical boundary conditions in a roughly linear fashion. The correlation between NR and viscosity ratios is slightly higher when the ratio between continental and oceanic regions is used. The NR component in the MM–NMR reference frame levels off at $\nu \sim 0.8$ and $\nu \sim 0.6$ for prescribed plate motions and free-slip models, respectively. Models without the additional buoyancy and rheology anomalies as imaged by seismic tomography within the 100–300 km depths thus produce less NR than the models discussed above ($\nu \approx 1$ for the free-slip $\eta(T, \dot{\epsilon})$ of Table 4). I take this as an indication that continental roots are the main cause for the excitation of NR. However, other effects such as regional slab dynamics, as suggested by Zhong (2001), may contribute ~ 40 per cent. The range

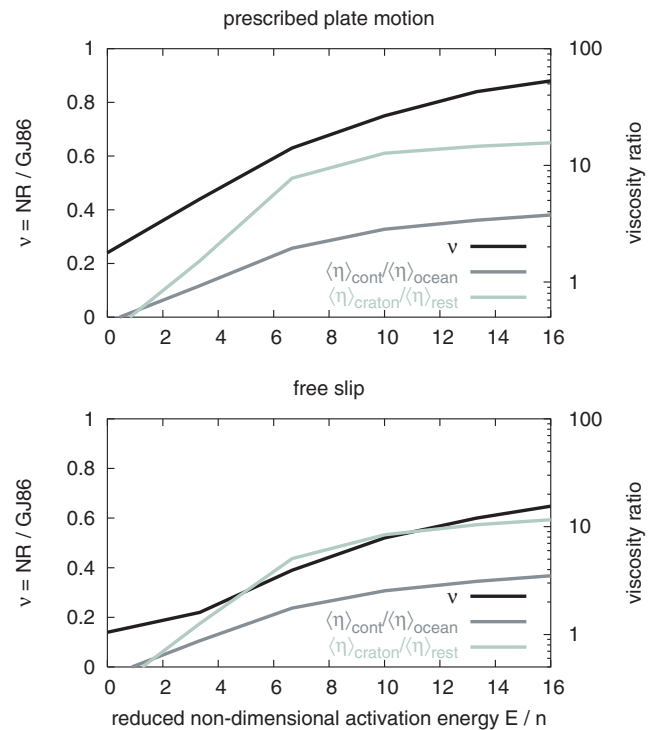


Figure 7. NR of the surface in MM–NMR reference frame normalized to GJ86, ν , and mean viscosity ratios for cratonic and continental regions between 100 and 250 km depth as a function of the E/n temperature-dependence parameters of viscosity law A. I show results for $\eta(T, \dot{\epsilon})$ computations without tomographic anomalies shallower than 300 km using prescribed surface velocities (top) and weak zone/free-slip (bottom figure).

of viscosity variations seen in the quasi-asymptotic part of Fig. 7 is consistent with theoretical arguments by O’Connell *et al.* (1991) and Ricard *et al.* (1991) that at least \sim one order of magnitude viscosity variations are required to generate NR of the lithosphere with magnitudes as observed in hotspot reference frames.

The deeper roots required in ZH01 to excite large NR amplitudes led to a decrease in the model fit to the geoid because of deep flow coupling. Čadež & Fleitout (2003) showed that a good match to the geoid could, however, be achieved with strong keels when flow is impeded across the 660 km phase transition. While I do not consider the geoid as a constraint here, I speculate that my models would be less affected by the detrimental coupling to the lower mantle for two reasons. First, it appears that my $\eta(T, \dot{\epsilon})$ models with heterogeneities due to seismic tomography lead to higher toroidal:poloidal partitioning and NR values for shallower continental roots than in ZH01. Second, the strain-rate weakening effect as shown in Fig. 7 may be expected to counteract the strongest rheological contrasts, and so reduce shear coupling. I leave further discussion of the detailed amplitudes and generation mechanisms of NR mechanisms for future study that should incorporate geoid constraints and more realistic plate formulations. However, my models refine earlier results and show that net motion is a robust feature of numerical models with LVVs.

The excitation of strong NR flow leaves us with a problem for models where surface velocities are prescribed, as commonly used for mantle flow modelling. As Figs 5(a) and 7 show, the deviations between model velocities based solely on NR components can become large at depths $\gtrsim 400$ km. Particular care should thus be taken if deep flow in the lower mantle is of importance (e.g. McNamara &

Zhong 2004). For my model choices, the lower mantle would lead the surface motions when they are prescribed in the NNR reference frame (Fig. 5a). If I had prescribed HS3 plate velocities, alternatively, the NR component induced by the plates alone would be stronger than the NR motion that would consistently arise from convection for free-slip models. At least for the present-day density structure, it appears that the lower mantle is relatively stable in a MM–NNR frame (Fig. 5b). For steady-state flow models, a plausible approach to ensure the lower mantle that has little NR motion would then be: First, compute the surface NR for a MM–NNR free-slip model. Second, prescribe this NR in addition to a NNR, relative plate velocity model at the surface. For temporally evolving mantle structure, this approach may be infeasible, however.

3.5 Fit to plate-tectonic surface motions

Lastly, Fig. 8 shows a comparison between the velocities of prescribed plate-motion and free-slip models after each velocity field was rotated into a MM–NNR reference frame. As expected from Figs 2 and 3, the velocities for both approaches are similar at the $\xi > 0.825$ correlation level at the surface, and at the $\xi > 0.9$ level below $z \gtrsim 250$ km. The increase of similarity with depth is expected, as buoyancy-driven flow will become dominant. Conversely, the mismatch of surface velocities may be attributed to the simplified weak-zone formulation of the free-slip models. This approximation clearly does not fully capture plate/plate boundary behaviour on Earth.

Models with LVVs due to temperature show larger ξ values and are more similar to present-day plate motions than the η_r models, including at lithospheric depths (Fig. 8 and Table 5). There are two reasons for this. First, $\eta(T)$ types of models can more appropriately describe plate-like behaviour and lead to smaller lateral velocity gradients within plates (e.g. Zhong *et al.* 1998; Tackley 2001b). Plateness, Π , (or the absence of intra-plate velocity gradients at the surface) is defined here by how well the surface velocities \mathbf{v} as interpolated from my flow computations can be fit by velocities due to rigid plate motions, \mathbf{w} . A total of $N = 64\,800$ velocities \mathbf{v} are gridded evenly in longitude–latitude space from the FE computations, and the \mathbf{w} are inverted for using the geometry of $M = 14$ large NUVEL-1 plates. This leads to M best-fit Euler vectors. For each

plate i with N_i velocities \mathbf{v}^i , an area-weighted, reduced $\hat{\chi}_i^2$ misfit is computed in a least-squares sense

$$\hat{\chi}_i^2 = \frac{1}{N_i - 3} \sum_{j=1}^{N_i} \frac{1}{\sin(\theta_j^i)} |\mathbf{v}_j^i - \mathbf{w}_j^i|^2. \quad (12)$$

Here, θ_j^i is the colatitude of velocity \mathbf{v}_j^i and the factor of three arises because of the three components of the i th Euler vector. Plateness can then be defined using the weighted sum of the misfits

$$\Pi = 1 - \hat{\chi}^2 = 1 - \sum_{i=1}^M A_i \hat{\chi}_i^2 \quad \text{where} \quad N = \sum_{i=1}^M N_i, \quad (13)$$

and A_i is the area of plate i normalized by the total surface area. For NUVEL-1, I find $\Pi \approx 1$, and velocity models with intra-plate deformation such as GSRM (Kreemer *et al.* 2003) have $\Pi \sim 0.9$ (Table 5).

In terms of plateness Π , some of the LVV models with T -dependent viscosity are more plate-like than the η_r case (Table 5); both $\eta(T)$ and η_{eff} lead to an increase of Π compared to η_r . This is because of the strong, near rigid-lid behaviour of temperature-dependent viscosity. The $\eta(T)$ surface velocities are in fact more plate-like than GSRM. Power-law flow for my simplified rheological law $\eta(T, \dot{\epsilon})$ reduces the plateness of $\eta(T)$ models by smoothing the velocity gradients, which are partly induced by the weak-zone geometry. Π for $\eta(T, \dot{\epsilon})$ is decreased, even when compared to η_r . Some of this reduction in plateness is due to deep-seated buoyancy-driven flow underneath oceanic plates; Π for a $\eta(T, \dot{\epsilon})$ model without suboceanic anomalies above 300 km is ≈ 0.7 . Using Π from GSRM as a reference, the η_{eff} model leads to the best plateness with $\Pi \sim 0.9$, very close to what is observed considering my limited resolution of plate boundary mechanics. Given the $T, \dot{\epsilon}$ -dependence of the joint rheology, most of the plates are in the cold, diffusion creep regime at the surface, leading to lower strain rates within. Only close to ridges do strain rates and temperatures allow for dislocation creep (*cf.* Podolefsky *et al.* 2004). However, the exact Π values should not be overinterpreted, as they may be affected by the size of weak zones or the viscosity cut-off.

A second reason for the improved ξ misfit is that LVVs preferentially speed up plates with large oceanic regions. This is seen in an increased surface rms speed ratio, Ω , of oceanic to continental regions (as defined based on the 3SMAC regionalization). For free-slip model η_r , $\Omega = 1.7$ and increases to 2.5–3.2 in the MM–NNR frame for models with temperature-dependent LVVs (Table 5). This compares well with observations, which are $\Omega \sim 2.8$ for plate motions models in hotspot reference frames, respectively. (Geodynamic model Ω values should be compared with hotspot reference frame estimates in Table 5 as the v surface NR component is included in the MM–NNR frame.) For the simpler structural model without tomographic anomalies within the upper 300 km, Ω is reduced to 2.1 from 2.5 for $\eta(T, \dot{\epsilon})$. While still significantly larger than Ω for η_r , this comparison shows that a substantial part of the speed up, and general modification of flow patterns underneath oceanic plates, is caused by relatively shallow density anomalies as inferred from tomography.

In summary, I find that the introduction of LVVs into large-scale, global circulation models leads to improved model fits to plate motions. In particular the η_{eff} model is Earth-like in terms of correlation with observed velocities, plateness, ocean/continent speed ratio, and toroidal flow diagnostics. Along with the modified drag coupling underneath continents as pointed out by Conrad & Lithgow-Bertelloni (2006), these findings imply that the analyses of Becker & O’Connell (2001) and Conrad & Lithgow-Bertelloni

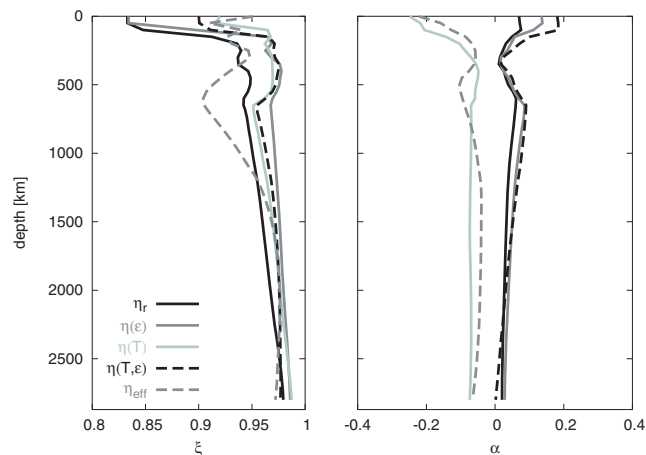


Figure 8. Comparison of velocities from surface plate-motion prescribed (reference) and free-slip/weak zone models for different rheologies in a mean NNR reference frame. Left subplot shows correlation, ξ ; right subplot amplitude ratio, α . Compare with Fig. 5, but note different x -axes.

(2004) should be repeated with modified circulation models. Here, I am mainly interested in checking the general consistency of the free-slip and velocity-prescribed approaches, in order to ensure that the conclusions about the effect of rheology are general. As the right part of Fig. 8 shows, the velocity amplitudes of the prescribed velocity models is matched quite well for most free-slip models, and $-0.2 \lesssim \alpha \lesssim 0.2$ for most models. This velocity match depends on the weak zone formulation (Yoshida *et al.* 2001) and could further be improved by adjusting the $dT/d \ln v_S$ scaling, which I picked based on previous flow modelling results (Becker & O'Connell 2001). The outliers in Fig. 8 are again the $\eta(T)$ and η_{eff} models which are affected by large surface viscosities, as discussed for Fig. 5.

4 CONCLUSIONS

In terms of the global structure of flow, models with LVV and power-law rheologies show velocities that are similar to those of Newtonian, or purely radially-varying viscosity models. Results are consistent with common notions built on earlier 2-D convection models (Christensen 1984). For studies that focus on the role of mantle flow on such large scales, rheological assumptions will likely only play a minor role in affecting global model conclusions. The story may be different if regional predictions of the flow models are considered. For these cases, the role of mantle rheology needs further study and may in fact be constrained by the application of improved global circulation models.

Substantiating earlier findings by Zhong (2001), excitation of a NR component of the lithosphere with respect to the lower mantle is a consequence of stiff continental roots and scales with the strength of the viscosity variations. The surface NR of my models matches hotspot reference-frame predictions well in terms of orientations. The amplitude of the predicted rotation is close to GJ86's estimates, but only \sim a third of the newer HS3 values. This discrepancy might partly be due to uncertainties about hotspot motion; they may be further addressed if subduction zones are incorporated into global flow models with a higher degree of realism. I find that NR of the lithosphere with respect to a stable lower mantle is a generic feature of models with LVV for both weak zone and prescribed plate motion models. This implies that care should be taken as to choosing a consistent reference frame when surface velocities are prescribed for mantle flow models, particularly if velocities deeper than \sim 500 km are of interest.

Global circulation models can be constructed with temperature and strain-rate dependent viscosity laws that are broadly consistent with laboratory findings on dry olivine rheology. These models produce predominantly dislocation creep in the uppermost mantle, which may explain that seismic anisotropy due to LPO is concentrated in the upper \sim 300 km. Density-driven models with weak zones match observed plate motions in terms of amplitudes and directions of flow. For the strongly temperature-dependent cases, LVV models lead to improved plate-like behaviour in terms of excited toroidal energy, ocean/continent speed ratios, and flatness of flow. This indicates that previous studies on the effect of boundary forces on plate motions may have to be revisited.

ACKNOWLEDGMENTS

I thank the reviewers C. Conrad, S. Zhong, and editor Jun Korenaga for their suggestions, R. Lara, R. J. O'Connell, B. Steinberger for comments on an earlier draft, J. Hernlund for discussions of toroidal flow, A. McNamara, J. van Hunen, and E. Tan for help with `Cit.com`,

M. Billen and G. Hirth for comments on rheology, S. Zhong, L. Moresi, M. Gurnis and others involved in the `geoframework.org` effort for sharing `Cit.com`. This material is based upon work supported by the National Science Foundation under Grant No. 0509722. Computations for the work described in this paper were conducted at the University of Southern California Center for High Performance Computing and Communications (www.usc.edu/hpcc). Most figures were produced with the GMT software by Wessel & Smith (1991).

REFERENCES

- Ashby, M.F. & Verrall, R.A., 1977. Micromechanisms of flow and fracture, and their relevance to the rheology of the upper mantle, *Phil. Trans. Roy. Soc. Lond.*, **A**, **288**, 59–95.
- Becker, T.W. & Boschi, L., 2002. A comparison of tomographic and geodynamic mantle models, *Geochemistry, Geophysics, Geosystems*, **3** (2001GC000168).
- Becker, T.W. & O'Connell, R.J., 2001. Predicting plate velocities with geodynamic models, *Geochemistry Geophysics Geosystems*, **2** (2001GC000171).
- Becker, T.W., Kellogg, J.B., Ekström, G. & O'Connell, R.J., 2003. Comparison of azimuthal seismic anisotropy from surface waves and finite-strain from global mantle-circulation models, *Geophys. J. Int.*, **155**, 696–714.
- Becker, T.W., Chevrot, S., Schulte-Pelkum, V. & Blackman, D.K., 2006a. Statistical properties of seismic anisotropy predicted by upper mantle geodynamic models, *J. geophys. Res.*, **111**, B08309, doi:10.1029/2005JB004095.
- Becker, T.W., Schulte-Pelkum, V., Blackman, D.K., Kellogg, J.B. & O'Connell, R.J., 2006b. Mantle flow under the western United States from shear wave splitting, *Earth planet. Sci. Lett.*, **247**, 235–251.
- Behn, M.D., Conrad, C.P. & Silver, P.G., 2004. Detection of upper mantle flow associated with the African Superplume, *Earth planet. Sci. Lett.*, **224**, 259–274.
- Bercovici, D., 1995. A source-sink model of the generation of plate-tectonics from non-Newtonian mantle flow, *J. geophys. Res.*, **100**, 2013–2030.
- Bercovici, D., Ricard, Y. & Richards, M., 2000. The relationship between mantle dynamics and plate tectonics: a primer, in *The History and Dynamics of Global Plate Motions*, Vol. 121, pp. 5–46, eds Richards, M., Gordon, R. & van der Hilst, R.D., Geophysical Monograph, American Geophysical Union, Washington, DC.
- Billen, M.I. & Hirth, G., 2005. Newtonian versus non-Newtonian upper mantle viscosity: implications for subduction initiation, *Geophys. Res. Lett.*, **32** (doi:10.1029/2005GL023457).
- Čadek, O. & Fleitout, L., 2003. Effect of lateral viscosity variations in the top 300 km of the mantle on the geoid and dynamic topography, *Geophys. J. Int.*, **152**, 566–580.
- Čadek, O., Ricard, Y., Martinec, Z. & Matyska, C., 1993. Comparison between Newtonian and non-Newtonian flow driven by internal loads, *Geophys. J. Int.*, **112**, 103–114.
- Chapple, W.M. & Tullis, T.E., 1977. Evaluation of the forces that drive the plates, *J. geophys. Res.*, **82**, 1967–1984.
- Christensen, U.R., 1984. Convection with pressure- and temperature-dependent non-Newtonian rheology, *Geophys. J. R. astr. Soc.*, **77**, 343–384.
- Christensen, U. & Harder, H., 1991. Three-dimensional convection with variable-viscosity, *Geophys. J. Int.*, **104**, 213–226.
- Conrad, C.P. & Lithgow-Bertelloni, C., 2004. The temporal evolution of plate driving forces: importance of 'slab suction' versus 'slab pull' during the Cenozoic, *J. geophys. Res.*, **109** (doi:10.1029/2004JB002991).
- Conrad, C.P. & Lithgow-Bertelloni, C., 2006. Influence of continental roots and asthenosphere on plate-mantle coupling, *Geophys. Res. Lett.*, **33** (doi:10.1029/2005GL02562).
- Dahlen, F.A. & Tromp, J., 1998. *Theoretical Global Seismology*, Princeton University Press, Princeton, New Jersey.

- DeMets, C., Gordon, R.G., Argus, D.F. & Stein, S., 1990. Current plate motions, *Geophys. J. Int.*, **101**, 425–478.
- Dumoulin, C., Bercovici, D. & Wessel, P., 1998. A continuous plate-tectonic model using geophysical data to estimate plate-margin widths, with a seismicity-based example, *Geophys. J. Int.*, **133**, 379–389.
- Dziewoński, A.M. & Anderson, D.L., 1981. Preliminary reference Earth model, *Phys. Earth planet. Inter.*, **25**, 297–356.
- Forsyth, D.W. & Uyeda, S., 1975. On the relative importance of the driving forces of plate motion, *Geophys. J. R. astr. Soc.*, **43**, 163–200.
- Forte, A.M. & Mitrovica, J.X., 2001. Deep-mantle high-viscosity flow and thermochemical structure inferred from seismic and geodynamic data, *Nature*, **410**, 1049–1056.
- Gable, C.W., O'Connell, R.J. & Travis, B.J., 1991. Convection in three dimensions with surface plates: generation of toroidal flow, *J. geophys. Res.*, **96**, 8391–8405.
- Gaboret, C., Forte, A.M. & Montagner, J.-P., 2003. The unique dynamics of the Pacific Hemisphere mantle and its signature on seismic anisotropy, *Earth planet. Sci. Lett.*, **208**, 219–233.
- Goetze, C. & Evans, B., 1979. Stress and temperature in the bending lithosphere as constrained by experimental rock mechanics, *Geophys. J. R. astr. Soc.*, **59**, 463–478.
- Gordon, R.G. & Jurdy, D.M., 1986. Cenozoic global plate motions, *J. geophys. Res.*, **91**, 12 389–12 406.
- Grand, S.P., 1994. Mantle shear structure beneath the Americas and surrounding oceans, *J. geophys. Res.*, **99**, 11 591–11 621.
- Grand, S.P., 2001. Updated tomographic model based on Grand (1994), Grand *et al.* (1997), accessed 02/2001, <ftp://amazon.geo.utexas.edu/outgoing/steveg/>.
- Grand, S.P., van der Hilst, R.D. & Widiyantoro, S., 1997. Global seismic tomography; a snapshot of convection in the Earth, *GSA Today*, **7**, 1–7.
- Gripp, A.E. & Gordon, R.G., 1990. Current plate velocities relative to the hotspots incorporating the NUVEL-1 global plate motion model, *Geophys. Res. Lett.*, **17**, 1109–1112.
- Gripp, A.E. & Gordon, R.G., 2002. Young tracks of hotspots and current plate velocities, *Geophys. J. Int.*, **150**, 321–361.
- Hager, B.H. & Clayton, R.W., 1989. Constraints on the structure of mantle convection using seismic observations, flow models, and the geoid, in *Mantle convection; plate tectonics and global dynamics*, Vol. 4, pp. 657–763, ed. Peltier, W.R., The Fluid Mechanics of Astrophysics and Geophysics, Gordon and Breach Science Publishers, New York, NY.
- Hager, B.H. & O'Connell, R.J., 1981. A simple global model of plate dynamics and mantle convection, *J. geophys. Res.*, **86**, 4843–4867.
- Hirth, G. & Kohlstedt, D.L., 2004. Rheology of the upper mantle and the mantle wedge: A view from the experimentalists, in *Inside the Subduction Factory*, Vol. 138, pp. 83–105, ed. Eiler, J., Geophysical Monograph, American Geophysical Union, Washington DC.
- Jordan, T.H., 1978. Composition and development of the continental tectosphere, *Nature*, **274**, 544–548.
- Karato, S.-i., 1998. Seismic anisotropy in the deep mantle, boundary layers and the geometry of convection, *Pure appl. Geophys.*, **151**, 565–587.
- King, S.D. & Hager, B.H., 1990. The relationship between plate velocity and trench viscosity in Newtonian and power-law subduction calculations, *Geophys. Res. Lett.*, **17**, 2409–2412.
- King, S.D., Gable, C.W. & Weinstein, S.A., 1992. Models of convection-driven tectonic plates: a comparison of methods and results, *Geophys. J. Int.*, **109**, 481–487.
- Kreemer, C., Holt, W.E. & Haines, A.J., 2003. An integrated global model of present-day plate motions and plate boundary deformation, *Geophys. J. Int.*, **154**, 5–34.
- Lenardic, A. & Moresi, L.-N., 1999. Some thoughts on the stability of cratonic lithosphere: effects of buoyancy and viscosity, *J. geophys. Res.*, **104**, 12 747–12 758.
- Lithgow-Bertelloni, C. & Richards, M.A., 1998. The dynamics of Cenozoic and Mesozoic plate motions, *Rev. Geophys.*, **36**, 27–78.
- Lithgow-Bertelloni, C., Richards, M.A., Ricard, Y., O'Connell, R.J. & Engebretson, D.C., 1993. Toroidal-poloidal partitioning of plate motions since 120 Ma, *Geophys. Res. Lett.*, **20**, 375–378.
- Martinez, Z., Matyska, C., Čadek, O. & Hrdina, P., 1993. The Stokes problem with 3-D Newtonian rheology in a spherical shell, *Comp. Phys. Comm.*, **76**, 63–79.
- McNamara, A.K. & Zhong, S., 2004. Thermochemical structures within a spherical mantle: superplumes or piles?, *J. geophys. Res.*, **109** (doi:10.1029/2003JB002847).
- McNamara, A.K., van Keken, P.E. & Karato, S.-I., 2003. Development of finite strain in the convecting lower mantle and its implications for seismic anisotropy, *J. geophys. Res.*, **108** (doi:10.1029/2002JB001970), 2230.
- Montagner, J.-P., 1998. Where can seismic anisotropy be detected in the Earth's mantle? In boundary layers, *Pure appl. Geophys.*, **151**, 223–256.
- Moresi, L. & Solomatov, V.S., 1995. Numerical investigations of 2D convection with extremely large viscosity variations, *Phys. Fluids*, **7**, 2154–2162.
- Müller, D., Roest, W.R., Royer, J.-Y., Gahagan, L.M. & Sclater, J.G., 1997. Digital isochrons of the world's ocean floor, *J. geophys. Res.*, **102**, 3211–3214.
- Nataf, H.-C. & Ricard, Y., 1996. 3SMAC: an *a priori* tomographic model of the upper mantle based on geophysical modeling, *Phys. Earth planet. Inter.*, **95**, 101–122.
- Nicolas, A. & Christensen, N.I., 1987. Formation of anisotropy in upper mantle peridotites; a review, in *Composition, structure and dynamics of the lithosphere-asthenosphere system*, Vol. 16, pp. 111–123, eds Fuchs, K. & Froidevaux, C., Geodynamics, American Geophysical Union, Washington DC.
- O'Connell, R.J., Gable, C.W. & Hager, B.H., 1991. Toroidal-poloidal partitioning of lithospheric plate motions, in *Glacial Isostasy, Sea-Level and Mantle Rheology*, pp. 535–551, ed. Sabadini, R., Kluwer Academic Publishers, Amsterdam.
- Ogawa, M., Schubert, G. & Zebib, A., 1991. Numerical simulations of three-dimensional thermal convection in a fluid with strongly temperature-dependent viscosity, *J. Fluid Mech.*, **233**, 299–328.
- Olson, P. & Bercovici, D., 1991. On the equipartitioning of kinematic energy in plate tectonics, *Geophys. Res. Lett.*, **18**, 1751–1754.
- Parmentier, E.M., 1978. A study of thermal convection in non-Newtonian fluids, *J. Fluid Mech.*, **84**, 1–11.
- Podolefsky, N.S., Zhong, S. & McNamara, A.K., 2004. The anisotropic and rheological structure of the oceanic upper mantle from a simple model of plate shear, *Geophys. J. Int.*, **158**, 287–296.
- Ranalli, G., 1995. *Rheology of the Earth*, 2nd Edn, Chapman & Hall, London.
- Ricard, Y. & Vigny, C., 1989. Mantle dynamics with induced plate tectonics, *J. geophys. Res.*, **94**, 17 543–17 559.
- Ricard, Y., Doglioni, C. & Sabadini, R., 1991. Differential rotation between lithosphere and mantle: a consequence of lateral mantle viscosity variations, *J. geophys. Res.*, **96**, 8407–8415.
- Ritzwoller, M.H., Shapiro, N.M. & Zhong, S., 2004. Cooling history of the Pacific lithosphere, *Earth planet. Sci. Lett.*, **226**, 69–84.
- Solomatov, V.S. & Moresi, L.-N., 1997. Three regimes of mantle convection with non-Newtonian viscosity and stagnant lid convection on the terrestrial planets, *Geophys. Res. Lett.*, **24**, 1907–1910.
- Stein, C., Schmalz, J. & Hansen, U., 2004. The effect of rheological parameters on plate behaviour in a self-consistent model of mantle convection, *Phys. Earth planet. Inter.*, **142**, 225–255.
- Steinberger, B., Sutherland, R. & O'Connell, R.J., 2004. Prediction of Emperor-Hawaii seamount locations from a revised model of global plate motion and mantle flow, *Nature*, **430**, 167–173.
- Tackley, P.J., 2001a. Self-consistent generation of tectonic plates in time-dependent, three-dimensional mantle convection simulations 1. Pseudoplastic yielding, *Geochemistry Geophysics Geosystems*, **1** (2000GC000036).
- Tackley, P.J., 2001b. Self-consistent generation of tectonic plates in time-dependent, three-dimensional mantle convection simulations 2. Strain weakening and asthenosphere, *Geochemistry Geophysics Geosystems*, **1** (2000GC000043).
- Trampert, J. & van Heijst, H.J., 2002. Global azimuthal anisotropy in the transition zone, *Science*, **296**, 1297–1299.
- Wang, S. & Wang, R., 2001. Current plate velocities relative to hotspots: implications for hotspot motion, mantle viscosity and global reference frame, *Earth planet. Sci. Lett.*, **189**, 133–140.

- Wen, L. & Anderson, D.L., 1997. Present-day plate motion constraint on mantle rheology and convection, *J. geophys. Res.*, **102**, 24 639–24 653.
- Wessel, P. & Smith, W.H.F., 1991. Free software helps map and display data, *EOS, Trans. Am. geophys. Un.*, **72**, 445–446.
- Wookey, J. & Kendall, J.-M., 2004. Evidence of midmantle anisotropy from shear wave splitting and the influence of shear-coupled P waves, *J. geophys. Res.*, **109** (doi:10.1029/2003JB002871).
- Yoshida, M., Honda, S., Kido, M. & Iwase, Y., 2001. Numerical simulation for the prediction of the plate motions: effects of lateral viscosity variations in the lithosphere, *Earth Planets Space*, **53**, 709–721.
- Zhang, S. & Christensen, U., 1993. Some effects of lateral viscosity variations on geoid and surface velocities induced by density anomalies in the mantle, *Geophys. J. Int.*, **114**, 531–547.
- Zhong, S., 2001. Role of ocean-continent contrast and continental keels on plate motion, net rotation of lithosphere, and the geoid, *J. geophys. Res.*, **106**, 703–712.
- Zhong, S. & Davies, G.F., 1999. Effects of plate and slab viscosities on geoid, *Earth planet. Sci. Lett.*, **170**, 487–496.
- Zhong, S., Gurnis, M. & Moresi, L., 1998. Role of faults, nonlinear rheology, and viscosity structure in generating plates from instantaneous mantle flow models, *J. geophys. Res.*, **103**, 15 255–15 268.
- Zhong, S., Zuber, M.T., Moresi, L. & Gurnis, M., 2000. Role of temperature-dependent viscosity and surface plates in spherical shell models of mantle convection, *J. geophys. Res.*, **105**, 11 063–11 082.

APPENDIX A: CONVERSION AND UNCERTAINTIES OF LABORATORY CREEP LAWS

Laboratory creep laws such as eq. (1) of Hirth & Kohlstedt (2004) (hereafter: HK03) are usually derived from uniaxial deformation experiments. The dependence of longitudinal strain rate, $\dot{\epsilon}_1$, on applied differential stress, σ , is commonly written in a form such as

$$\dot{\epsilon}_1 = A\sigma^n d^{-m} f(C_{OH}, \alpha) \exp\left(-\frac{E^* + pV^*}{RT}\right), \quad (\text{A1})$$

where C_{OH} and α indicate water and melt-content, respectively, and $f(C_{OH}, \alpha)$ stands for the function describing this dependency, for example, the parametrization of HK03. We wish to convert eq. (A1) into a viscosity law such as eq. (4) that uses the second strain-rate invariant, $\dot{\epsilon}_{II}$, and is cast in terms of the deviatoric stress, τ_{ij} , and strain rate, $\dot{\epsilon}_{ij}$, tensors. Based on the regular definition of the strain-rate tensor

$$\dot{\epsilon}_{ij} = \frac{1}{2} \left(\frac{\partial u_i}{\partial x_j} + \frac{\partial u_j}{\partial x_i} \right) \quad (\text{A2})$$

(where $\partial u_i / \partial x_j$ indicates the spatial derivative in j of velocities in i direction) and viscosity

$$\tau_{ij} = 2\eta\dot{\epsilon}_{ij}, \quad (\text{A3})$$

a factor of $3^{(n+1)/2}/2$ then arises (e.g. Ranalli 1995, eq. 4.25). Including a conversion of HK03's A factor to SI units, the rheological law correction, and the water content dependency, we can write

$$\begin{aligned} A' &= \frac{3^{(n+1)/2}}{2^{1-n}} 10^{-6(m+n)} C_{OH}^r A \quad \text{for wet conditions, and} \\ &= \frac{3^{(n+1)/2}}{2^{1-n}} 10^{-6(m+n)} A \quad \text{for dry.} \end{aligned} \quad (\text{A4})$$

Here, C_{OH} is the water content in $\text{H}/10^6\text{Si}$, r a constant ($r = 1$ for diffusion, and $r = 1.2$ for dislocation creep) and A the constants for both water-content cases from Table 1 of HK03. Units of A' are $\text{Pa}^{-n} \text{m}^m \text{s}^{-1}$.

HK03 give A parameters of $1.5 \cdot 10^9$ and $1.1 \cdot 10^5$ for dry diffusion and dislocation creep of olivine according to eq. (A1). With the conversion rule eq. (A4) and m and n values from Table 3 this translates to A' values of $4.5 \cdot 10^{-15}$ and $7.4 \cdot 10^{-15}$ for diffusion and dislocation creep, respectively. These dry A' values were used in Table 3 for the effective viscosity law η_{eff} which led to moderately good agreement between the reference η_r profile and the laboratory-derived creep law as discussed in the main text. For wet rheologies at constant $C_{OH} = 1000$, I convert HK03's A values to A' values of $3 \cdot 10^{-15}$ and $2.4 \cdot 10^{-14}$ for diffusion and dislocation creep, respectively. Those wet values led to a strong viscosity drop at upper mantle depths, as mentioned in the main text, and were not considered further for this study.

One should be cautious before drawing any detailed conclusions from the exact findings for different laboratory-derived creep laws involving factors such as A' . In practical terms, the A pre-factors of laboratory results such as those compiled in Hirth & Kohlstedt (2004) are probably the least well-constrained creep law parameters. The A values of HK03 may be uncertain to within a factor of ~ 6 or so (G. Hirth, personal communication, 2006). Moreover, V^* for η_{diff} is not well constrained, which limits the reliability of the depth dependence of my viscosity law B. In terms of the partitioning between dislocation and diffusion creep as shown in Fig. 4(a), an important control is the grain size d . The d parameter affects the value of the diffusion creep viscosity strongly, and hence co-determines the location and transition depth between regions where η_{diff} or η_{dist} is dominant (e.g. Ranalli 1995). While natural samples lead us to expect d to be of order 1–10 mm, d might well vary with depth in the upper mantle, and over time during progressive deformation. There are also other well-known uncertainties with regard to the applicability of laboratory creep laws, among them the issue that the mantle is not pure olivine. My rheological model η_{eff} should thus not be considered as an attempt to simulate the mantle, but as a test of a joint rheologies whose dependency on p and T are likely similar to the creep behaviour of the mantle. In this sense, I expect my findings to be robust.